ORBITAL DYNAMICS FOR A NON-PERFECTLY REFLECTING SOLAR SAIL CLOSE TO AN ASTEROID

Ariadna Farrés[*], Àngel Jorba[†], and Josep-Maria Mondelo[‡]

In this paper we focus on a mission scenario of a solar sail close to an asteroid. We consider the Augmented Hill Three Body problem as a model, where the asteroid is considered as a point mass and both the effect of solar tides and the solar radiation pressure due to the solar sail are included. We will give a complete description of the most relevant dynamics properties of the system. We will compute families of periodic and quasi-periodic orbits for different fixed sail orientations.

INTRODUCTION

In the past two decades there has been a tremendous activity in the study of small bodies (asteroids and comets) mainly due to their unique nature as remnants of the early stages of the Solar System formation and also as a detailed record of its evolution up to present time. More recently, these objects have also been recognised as both a possible threat for the Earth (potential collisions) and stepping stones for human exploration beyond low-Earth orbits (manned mission to asteroids for asteroid mining).

On the other hand, solar sailing is considered a cheap way to travel around space, and could enable multi-rendezvous mission towards different target asteroids.[1] Moreover, due to their small gravitational field, solar radiation pressure (SRP) plays an important role on the dynamics around asteroids.[2] Hence, the systematic use of SRP to propel a satellite via specialised reflecting areas, such as solar sails, can give rise to new and interesting mission concepts.

When we study the dynamics of a satellite close to an asteroid there are three effects that must be considered: its gravitational field, solar tides and solar radiation pressure (SRP). The first effect accounts for the shape and spin states of the asteroid, and is relevant within a few radii from its surface, in what is known as the gravity regime. Far from the gravity regime, considering the asteroid as a point mass provides a good approximation. Here effects like the SRP and the Sun's gravity are more relevant and must be taken into account.

In this paper we will focus on a mission scenario of a solar sail close to Ceres. We will consider an imperfect flat solar sail, that accounts for both the reflectivity and absorption of the sail's material. We will use the Augmented Hill 3-body problem as a dynamical model, where the asteroid is considered as a point mass and the effect of SRP due to the solar sail is added. We will give a

---

[*]Postdoc Researcher, Departament de Matemàtica Aplicada i Anàlisi, Universitat de Barcelona, Gran Via de les Corts Catalanes 585, 08007 Barcelona, Spain

[†]Professor, Departament de Matemàtica Aplicada i Anàlisi, Universitat de Barcelona, Gran Via de les Corts Catalanes 585, 08007 Barcelona, Spain

[‡]Associate Professor, Departament de Matemàtiques, Universitat Autónoma de Barcelona, Bellaterra 08193 (Barcelona), Spain.

complete description of the most relevant dynamical properties of the system (i.e. fixed points, periodic and quasi-periodic orbits, ...). Finally we will discuss their possible applications to asteroid mission analysis.

THE AH3BP MODEL FOR A NON-PERFECTLY REFLECTING SOLAR SAIL

To capture the dynamics of a solar sail around an asteroid we use the Augmented Hill 3-Body problem (AH3BP), which models the motion of two small masses (asteroid and spacecraft) that interact due to their mutual gravitational attraction and is perturbed by a distant large body (the Sun). The AH3BP also takes into account the effect of SRP due to the solar sail.[3,4] As the Sun–sail distance is large compared to the asteroid–sail distance, the effect of the Sun is included as a uniform gravity field and a uniform SRP, both in the horizontal direction.

We consider a rotating reference frame centred on the small body, defined such that: the x direction points from the Sun to the asteroid; the z direction is aligned with the Sun–asteroid angular velocity; and the y direction completes a positive coordinate system. We normalise units in such a way that the unit of distance, L, is $(\mu_{sb}/\mu_{sun})^{1/3}R$, and the unit of time, T, is $1/\omega$, where μ_{sun} is the gravitational parameter of the Sun ($\approx 1.327 \times 10^{11} \text{km}^3/\text{s}^2$), μ_{sb} is the gravitational parameter of the smaller body, R is the mean distance between the Sun and the asteroid, and $\omega = \sqrt{\mu_{sun}/R^3}$ is the angular velocity. Using these normalised units, the equations of motion for the AH3BP for a solar sail[5,2] are:

$$\ddot{X} - 2\dot{Y} = \frac{\partial \Omega}{\partial X} + a_X, \quad \ddot{Y} + 2\dot{X} = \frac{\partial \Omega}{\partial Y} + a_Y, \quad \ddot{Z} = \frac{\partial \Omega}{\partial Z} + a_Z. \tag{1}$$

with

$$\Omega(X, Y, Z) = \frac{1}{r} + \frac{1}{2}(3X^2 - Z^2),$$

(X, Y, Z) denotes the position of the solar sail in the rotating frame, $r = \sqrt{X^2 + Y^2 + Z^2}$ is the distance between the solar sail and the centre of the asteroid, and $\mathbf{a_{sail}} = (a_X, a_Y, a_Z)$ is the acceleration given by the solar sail.

To model the acceleration of the solar sail we use a simplified model for a non-perfectly reflecting (SNPR) solar sail,[6] which only takes into account absorption and reflection of the sail material. If we denote by a the absorption coefficient and by ρ the reflectivity coefficient, we have $a + \rho = 1$. The force due to absorption and reflection is given by $\mathbf{F_a} = PA\langle\mathbf{r_s}, \mathbf{n}\rangle\mathbf{r_s}$ and $\mathbf{F_r} = 2PA\langle\mathbf{r_s}, \mathbf{n}\rangle^2\mathbf{n}$ respectively. In the previous expressions, $P = P_0(R_0/R)^2$ is the SRP magnitude at a distance R from the Sun ($P_0 = 4.563\mu\text{N/m}^2$, the SRP magnitude at $R_0 = 1\text{AU}$), A is the area of the solar sail, $\mathbf{r_s}$ is the direction of SRP ($\mathbf{r_s} = (1, 0, 0)$ in the rotating reference frame) and $\mathbf{n}$ is the normal direction to the surface of the sail. Hence, the acceleration for the SNPR solar sail is given by:

$$\mathbf{a_{sail}} = \frac{2PA}{m}\langle\mathbf{r_s}, \mathbf{n}\rangle \left(\rho\langle\mathbf{r_s}, \mathbf{n}\rangle\mathbf{n} + \frac{1}{2}(1 - \rho)\mathbf{r_s}\right). \tag{2}$$

Notice that, $\rho = 1$ corresponds to a perfectly reflecting solar sail, and $\rho = 0$ to a perfect solar array where the absorption of the solar panels is the only effect. According to Dachwald et al.,[6] a solar sail with a highly reflective aluminium-coated side has an estimated value of $\rho \approx 0.88$.

We will parametrise the normal direction to the surface of the sail using two angles α, δ, representing the horizontal and vertical displacement with respect to $\mathbf{r_s}$, hence $\mathbf{n} = (\cos\alpha\cos\delta, \sin\alpha\cos\delta, \sin\delta)$.

As the sail cannot point towards the Sun, we have that $\alpha, \delta \in [-\pi/2, \pi/2]$. Finally, the efficiency of a solar sail is measured in terms of $\beta = 2PA/m$, also know as the sail lightness number. One can check that, with these definitions, the acceleration for the solar sail in Eq. (2) is written as

$$
\begin{aligned}
a_X &= \bar{\beta}(\rho \cos^3 \alpha \cos^3 \delta + 0.5(1 - \rho) \cos \alpha \cos \delta), \\
a_Y &= \bar{\beta}(\rho \cos^2 \alpha \cos^3 \delta \sin \alpha), \\
a_Z &= \bar{\beta}(\rho \cos^2 \alpha \cos^2 \delta \sin \delta),
\end{aligned}
\tag{3}
$$

where $\bar{\beta} = \beta(\mu_{sb}\omega^4)^{-1/3}$ is the sail lightness number in normalised units.[5]

Finally, we must mention that the system given by Equation 1 admits an integral of motion, also known as the Jacobi constant,

$$
J_c = \dot{X}^2 + \dot{Y}^2 + \dot{Z}^2 - 2\Omega(X, Y, Z).
\tag{4}
$$

Some comments on the normalised units

To derive the equations of motion for the AH3BP, we have considered a set of normalised units. We recall that the unit of length is defined as $L = (\mu_{sb}/\mu_{sun})^{1/3}R$, and the unit of time is defined as $T = 1/\omega$. Notice that they both depend on the target asteroid for our mission. In Table 1 we summarise the physical data for 4 different asteroids*, as well as the associated normalised units of distance and time of the AH3BP. We also include for each asteroid its orbital period, the sidereal rotational period and its maximum radius both in km and normalised units. We will use the maximum radii to provide an estimate of the gravity regime (which is around 3 to 4 times the asteroids' radii) for each asteroid. Notice that, for all the asteroids considered, the radius distance varies between 0.001 and 0.005.

Table 1. Relevant parameters for different asteroids

Asteroid	μ_{sb} (km^3/s^2)	R (AU)	UD (km)	UT (day)	Rot. Period	RADII (km/UD)
Eros	4.463×10^{-4}	1.45	3265.4	102.2	0.2194 days	8.42 (2.5×10^{-3})
Vesta	17.8	2.36	180782	210	0.2226 days	265 (1.4×10^{-3})
Ceres	63.2	2.767	321966.593	265.95	0.3781 days	487.3 (1.51×10^{-3})
Itokawa	2.1×10^{-9}	1.32	49.57	88.15	0.5055 days	0.165 (3.3×10^{-3})

The normalised sail lightness number is $\bar{\beta} = \beta(\mu_{sb}\omega^4)^{-1/3}$. We recall that $\beta = 2PA/m$, $\omega = \sqrt{\mu_{sun}/R^3}$ and $P = P_0(R_0/R)^2$. Taking this into account, we can rewrite $\bar{\beta}$ as

$$
\bar{\beta} = \frac{2P_0 R_0^2 (A/m)}{\mu_{sun}^{2/3}\mu_{sb}^{1/3}} = K_1(A/m)\mu_{sb}^{-1/3},
\tag{5}
$$

where $K_1 \approx 7.8502$ if A is given in m^2 and m in kg.[7] Hence, the value of $\bar{\beta}$ depends on both: $\sigma = (A/m)$, the area-to-mass ratio of the satellite, and μ_{sb}, the gravitational parameter of the small body. We could have the same $\bar{\beta}$ for two completely different missions scenarios. Notice that $\bar{\beta}$ is inversely proportional to $\mu_{sb}^{1/3}$. Hence, for a fixed area-to-mass ratio, the smaller the asteroid the larger the effect of SRP will be.

In Figure 1 we show the contour levels of the normalised sail lightness number $\bar{\beta}$ as a function of σ and μ_{sb}. As we can see, for small asteroids ($\mu_{sb} \approx 10^{-9}$) and an area-to-mass ratio of a regular
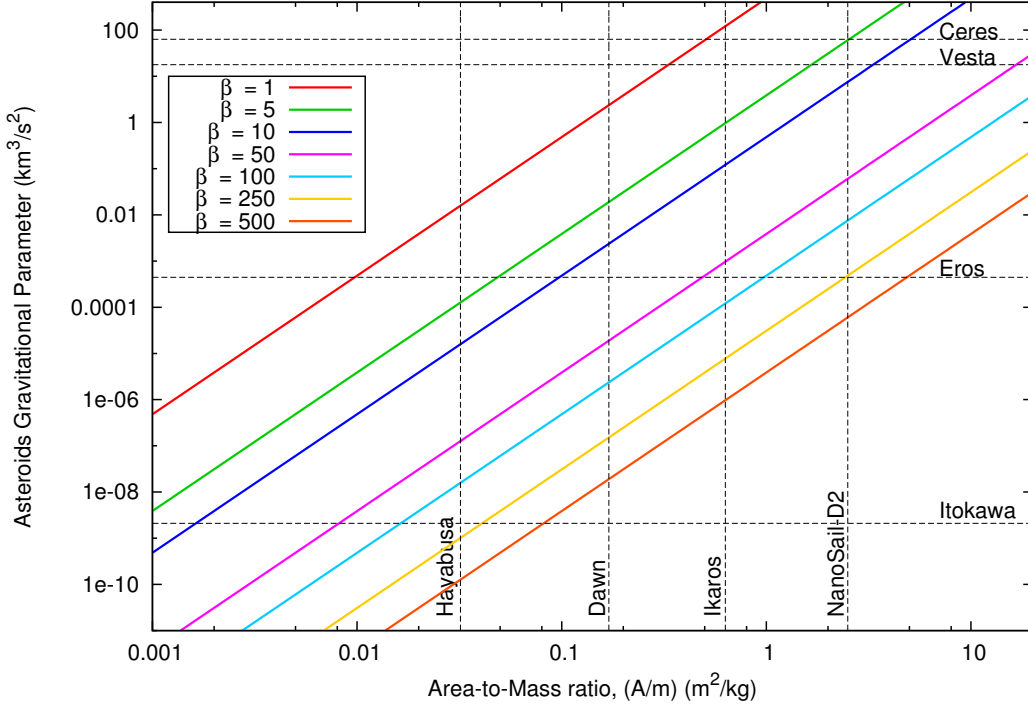
---

*The physical parameters have been taken from `http://ssd.jpl.nasa.gov/sbdb.cgi`

Figure 1. Contours of $\bar{\beta}$ as a function of (A/m), area-to-mass ratio, and μ_{sb}, the gravitational parameter of the asteroid.

spacecraft ($\sigma \approx 0.01$), $\bar{\beta}$ takes values between 50 and 100, whereas, for larger asteroids such as Ceres and Vesta ($\mu_{sb} \geq 10$) and a regular spacecraft this effect is very small ($\bar{\beta} \leq 0.03$).

In Table 2 we summarise the values of $\bar{\beta}$ for the 4 asteroids that appear in Table 1 and different area-to-mass ratios. As examples, we have taken the estimated area-to-mass ratio from Ikaros ($\sigma \approx 0.63 \text{m}^2$/kg), NanoSail-D2 ($\sigma \approx 2.5 \text{m}^2$/kg), Hayabussa ($\sigma \approx 0.032 \text{m}^2$/kg) and Dawn ($\sigma \approx 0.17 \text{m}^2$/kg). Although Hayabussa and Dawn are not solar sails, they have very large solar panels which could be considered for orbital control.[2] In Table 2 we see again how around a very small asteroid like Itokawa SRP is very important, even for spacecrafts like Hayabussa and Dawn.

Table 2. Normalised values for $\bar{\beta}$ for different mission configurations

	Ikaros ($\approx 0.63 \text{m}^2$/kg)	NanoSail-D2 ($\approx 2.5 \text{m}^2$/kg)	Hayabussa ($\approx 0.032 \text{m}^2$/kg)	Dawn ($\approx 0.17 \text{m}^2$/kg)
Eros	64.71	256.809	3.287	17.463
Vesta	1.894	7.51647	0.0962	0.511
Ceres	1.22	4.92	0.063	0.33
Itokawa	3862.02	15325.48	196.166	1042.13

In this paper we will focus on the particular case of a solar sail with similar characteristics as Nano-Sail and considering Ceres as target asteroid. Hence, we will consider $\bar{\beta} = 5$ and take a conservative value for the reflectivity coefficient, $\rho = 0.85$. We will describe the natural dynamics of the system, finding fixed points, periodic and quasi-periodic orbits for different fixed sail orientations.

4

EQUILIBRIUM POINTS

It is well know that thanks to the effect of a solar sail we can "artificially" displace the classical equilibrium points. In this section we will briefly describe the families of equilibrium points that appear in the AH3BP for $\bar{\beta} \in [1, 7]$ and $\rho = 0.85$. For further details see.[3,4,8]

We recall that when we neglect the effect of the solar sail ($\bar{\beta} = 0$) the system has two equilibrium points L_1, L_2 symmetrically located around the origin, with coordinates $(\pm 3^{-1/3}, 0, 0)$. When we include the SRP ($\bar{\beta} \neq 0$) but keep the sail perpendicular to the Sun–line ($\alpha = \delta = 0$), the position of L_1 and L_2 move along the x-axis towards the Sun as we increase the value of $\bar{\beta}$, having for $\bar{\beta} = 7$ $SL_1 = (-2.3916, 0, 0)$ and $SL_2 = (0.352, 0, 0)$. If, for a fixed $\bar{\beta}$, we change the sail orientation we will displace the position of the equilibrium points. Changes in α imply shifting the equilibrium point to one side or the other of the Sun–asteroid line, while changes in δ imply displacing the equilibrium point above or below the ecliptic plane.
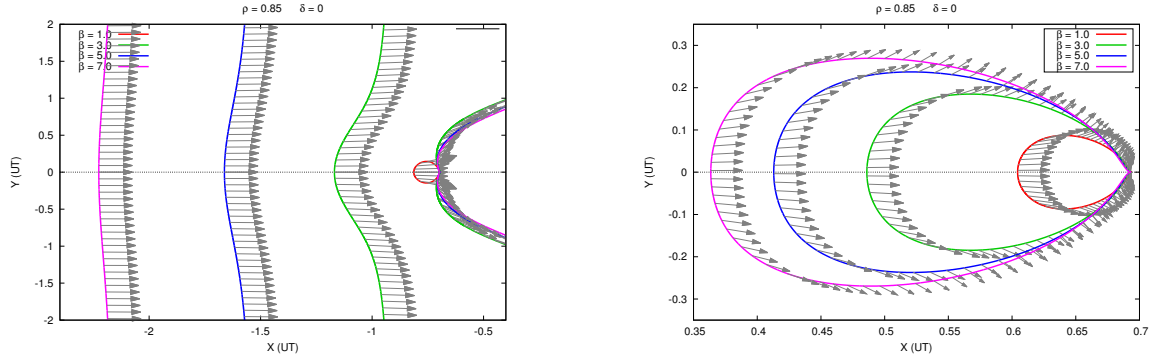

Figure 2. Family of equilibrium points for $\bar{\beta} = 1, 3, 5, 7$, $\alpha \in [-\pi/2, \pi/2]$ and $\delta = 0$. All the equilibria lie on the orbital plane $Z = 0$. Left: Points related to L_1, Right: Points related to L_2. The arrows represent the normal direction to the surface of the sail at each equilibrium point.
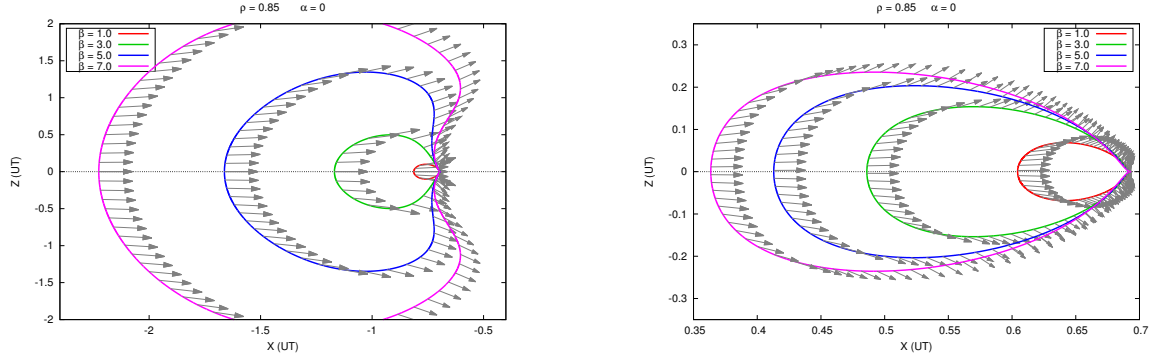

Figure 3. Family of equilibrium points for $\bar{\beta} = 1, 3, 5, 7$, $\alpha = 0$ and $\delta \in [-\pi/2, \pi/2]$. All the equilibria lay on the plane $Y = 0$. The arrows represent the normal direction to the surface of the sail at each equilibrium point.

In Figures 2 and 3 we show the position of the families of equilibria related to L_1 (left) and L_2 (right) for $\bar{\beta} = 1, 3, 5$ and 7. In Figure 2, the equilibria correspond to $\alpha \neq 0, \delta = 0$ and they all lie on the $Z = 0$ plane, whereas in Figure 3 they correspond to $\alpha = 0, \delta \neq 0$, i.e. they all on the $Y = 0$ plane. In both figures, the arrows represent, for each equilibrium point, the normal direction

to the surface of the solar sail. Notice that close to L_1, the points where the solar sail is almost perpendicular to the SRP are far from the asteroid, while for the equilibria close to L_2 those are the ones closer to the asteroid. Moreover, we know that the sail looses most of its efficiency if we tilt it more than $45°$, which makes us discard the equilibria close to L_1 and L_2 where the sail is almost edged off.

If we look at the stability of these equilibria we see that all the equilibrium points on the L_2 family are linearly unstable and their linear dynamics is centre×centre×saddle. On the other hand, although most of the equilibria on the L_1 family are of the same type, we also find some equilibria that are linearly stable on the ecliptic plane, with a linear dynamics of the type centre×centre×centre. These last type of equilibria appear for large $\bar{\beta}$ on the $Z = 0$ plane and far from the Sun-asteroid line.

In the case of a mission application where a solar sail is placed on an equilibrium point in order to monitor an asteroid, we are interested on points relatively close to the asteroid and on the day side of the asteroid. This brings our first dilemma: if we consider the equilibria that are closer to the surface of the asteroid these belong to the L_2 family, but they are on its dark side. On the other hand, if we consider the equilibria that are on the asteroid's day side, they belong to the L_1 family but are far away from the asteroid. For this reason, from now on, we will focus on the dynamics around the L_2 family of equilibria.

PERIODIC MOTION

As we have mentioned in the previous section, for most of the equilibrium points the linear dynamics is centre×centre×saddle. This means that under generic non-resonant conditions, two families of periodic orbits emanate from each fixed point (Lyapunov's Centre Theorem[9]). Each family is related to one of the two pairs of complex eigenvalues $(\pm\mathrm{i}\omega_1, \pm\mathrm{i}\omega_2)$ and the period of the orbits tends to $2\pi/\omega_i$ when we approach the equilibrium point.

In this section we will describe these families of periodic orbits for $\bar{\beta} = 5$, $\rho = 0.85$ and we will focus the region close to SL_2 (i.e. the displaced equilibrium point for $(\alpha_0, \delta_0) = (0, 0)$). As a representative set of angles, we have chosen $(\alpha_0, \delta_0) = (0.1, 0), (0.25, 0), (0.5, 0), (0, 0.1), (0, 0.25)$ and $(0, 0.5)$ (in radians). But here we only show the results for $(0, 0), (0.25, 0)$ and $(0, 0.25)$, as we observe similar results for each set of angle with $\alpha \neq 0, \delta \neq 0$. For each fixed sail orientation we have one displaced equilibrium point close to SL_2, where the linear dynamics is centre×centre×saddle (i.e. has $\{\pm\lambda, \pm\mathrm{i}\omega_1, \pm\mathrm{i}\omega_2\}$ as eigenvalues). Each complex eigenvalue is related to one of the two families of periodic orbits. The first one $(\pm\mathrm{i}\omega_1)$ will be related to the family of orbits with less out-of-plane displacement (Planar family) and the second one $(\pm\mathrm{i}\omega_1)$ to the family with maximum out-of-plane displacement (Vertical family).

To compute the families of periodic orbits for the different sail orientations, we need to take appropriate Poincaré sections to ensure the transversality of the flow. If (x_0, y_0, z_0) are the coordinates of the equilibrium point for (α_0, δ_0), we consider as Poincaré sections $\Gamma_1 = \{x_0 Y - y_0 X = 0, \quad x_0 \dot{Y} - y_0 \dot{X} > 0\}$. For each family of periodic orbits we use the linear approximation of the flow around (x_0, y_0, z_0) to compute the first orbit in the family. We use a continuation method to compute the rest of the orbits in the family.[10]

In Figure 4 we have the continuation diagram for the two families of periodic orbits given by $(\alpha = 0, \ \delta = 0)$ (left), $(\alpha = 0.25, \ \delta = 0)$ (middle) and $(\alpha = 0, \ \delta = 0.25)$ (right). Each point on the plot corresponds to the X and Z components of a periodic orbit on the Poincaré section Γ_1. We

have assigned a colour to each periodic orbit according to their linear normal dynamics: blue stands for centre×saddle, red stands for saddle×saddle and green stands for centre×centre.
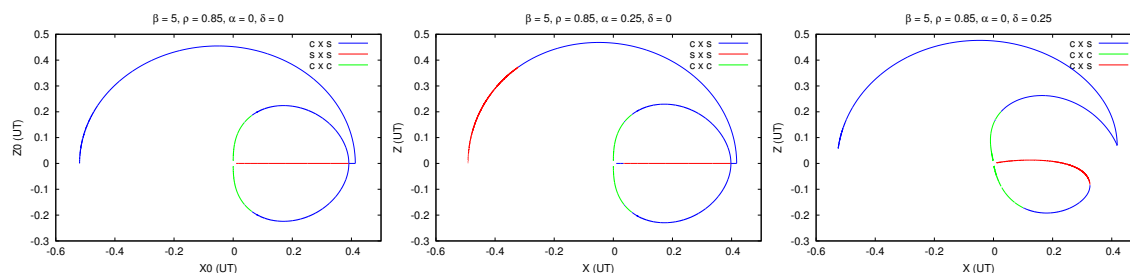

Figure 4. **For** $\bar{\beta} = 5, \rho = 0.85$**,** $(\alpha = 0, \ \delta = 0)$ **left,** $(\alpha = 0.25, \ \delta = 0)$ **middle,** $(\alpha = 0, \ \delta = 0.25)$ **right. Continuation diagram of the families of periodic orbits on the Poincaré section** Γ_1**,** $x_0 \ vs \ z_0$**.**

As we can see on the left hand side of Figure 4, for $\alpha = 0, \delta = 0$ we start with a planar family and a vertical family of periodic orbits, both unstable (centre×saddle). The vertical family of periodic orbits starts to gain Z amplitude as we move along it, and at some point the Z amplitude starts to decrease. On the other hand, the planar family is always contained in the orbital plane ($Z = 0$). At some point, the stability of planar orbits changes to saddle×saddle. There two families of Halo-type orbits are born. The Halo orbits that appear are also unstable centre×saddle. As we move along the family, the orbits get closer to the asteroid ($x_0 \to 0$), and at some point the orbits become stable (centre×centre).

If we take a sail orientation with $\alpha \neq 0, \delta = 0$ (Figure 4 middle), we find the same orbit distribution. We have a family of planar and vertical periodic orbits, and at some point the planar family changes its stability and two Halo orbits appear. The main difference between the two diagrams relies on the stability of the orbits. As we can see, both the planar and vertical families of periodic orbits change their stability when reaching the end of the family. On the other hand, when we take sail orientations with $\alpha = 0, \delta \neq 0$, we have a more drastic change on the orbit distribution (Figure 4 right). As we can see, there are two families of periodic orbits that are born from the fixed points. The vertical family has a similar behaviour, it starts gaining Z amplitude as we move along the family. On the other hand, the planar family has some vertical displacement, these orbits look more likely to be Halo-type orbits. As we move along the family these orbits get close to the asteroid ($x_0 \to 0$) and at some point the orbits turn stable. The "planar" type orbits and the other "Halo" type orbits have not disappeared. They are still there but they are related in different way. The same phenomena is found in the RTBP with solar sail.[11]

In Figures 5, 6 and 7 we have the X, Y, Z projections of the Planar Lyapunov, Vertical Lyapunov and Halo families of periodic orbits respectively. We can see how taking sail orientations with $\alpha \neq 0$ does not vary the shape of the orbits, it just displaces them with respect to the Sun–asteroid line. On the other hand, taking sail orientations with $\delta \neq 0$ makes the trajectory shift above the ecliptic plane. Finally notice that for $\delta \neq 0$ there are some Halo type orbits that do not persist (Figure 7).

Another way to classify the periodic orbits is by means of their orbital period τ or the Jacobi constant J_c, that gives us an idea of at what energy level the orbits exist. At the top of Figure 8 we have shown the period τ vs J_c for each of the families of periodic orbits. As in Figure 4, we have associated a colour to each orbit according to its stability. As we can see, for the planar and vertical families of orbits, as we move along the family, the period and energy increase. On the other hand,
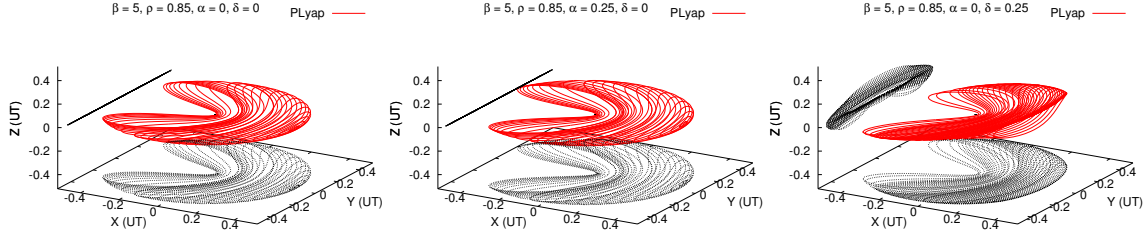
Figure 5. Families of Planar Lyapunov type orbits for $\beta = 5, \rho = 0.85$. From right to left: $(\alpha = 0, \ \delta = 0)$**,** $(\alpha = 0.25, \ \delta = 0)$ **and** $(\alpha = 0, \ \delta = 0.25)$**.**
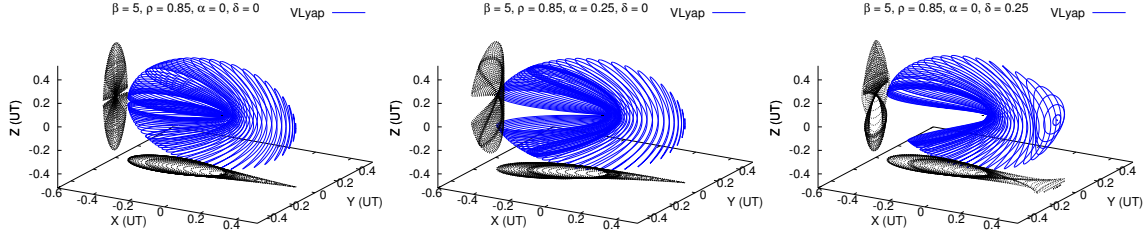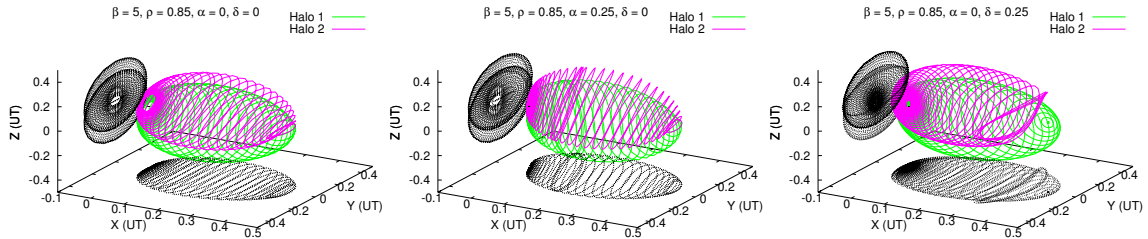

Figure 6. Families of Vertical Lyapunov type orbits for $\beta = 5, \rho = 0.85$. From right to left: $(\alpha = 0, \ \delta = 0)$**,** $(\alpha = 0.25, \ \delta = 0)$ **and** $(\alpha = 0, \ \delta = 0.25)$**.**

Figure 7. Families of Halo type orbits for $\beta = 5, \rho = 0.85$. From right to left: $(\alpha = 0, \ \delta = 0)$**,** $(\alpha = 0.25, \ \delta = 0)$ **and** $(\alpha = 0, \ \delta = 0.25)$**.**

for the Halo-type orbits, they both start to grow, but at some point they decrease drastically, having periods that tend to zero as we get closer to the asteroid, and very low energy values.

On the bottom of Figure 8 we show the period of the orbit vs the *stability parameters* s_1, s_2, which allows us to study the stability of the orbit and have estimates of the instability rate.[12] We recall that the spectrum of the state transition matrix of the a periodic orbit, $M(T)$, is $\{1, 1, \lambda_1, \lambda_1^{-1}, \lambda_2, \lambda_2^{-1}\}$, and we we define the *stability parameters* as $s_i = \lambda_i + \lambda_i^{-1}$. Notice that if $|s_i| > 2$ we have an unstable direction and if $|s_i| < 2$ we have a stable one. In these plots, the colour correspond to the type of orbit, blue for the Vertical Lyapunov type orbits, red for the Planar Lyapunov type orbits and green for the Halo type orbits. Notice how, all three type of orbits start being very unstable, with $s_1 \geq 1000$ and this decreases as the orbits get closer to the asteroid.

QUASI-PERIODIC MOTION

The linear dynamics of the equilibrium point is of the type centre$\times$centre$\times$saddle. Due to the saddle effect, almost all trajectories starting near the equilibrium point escape after a short time. On
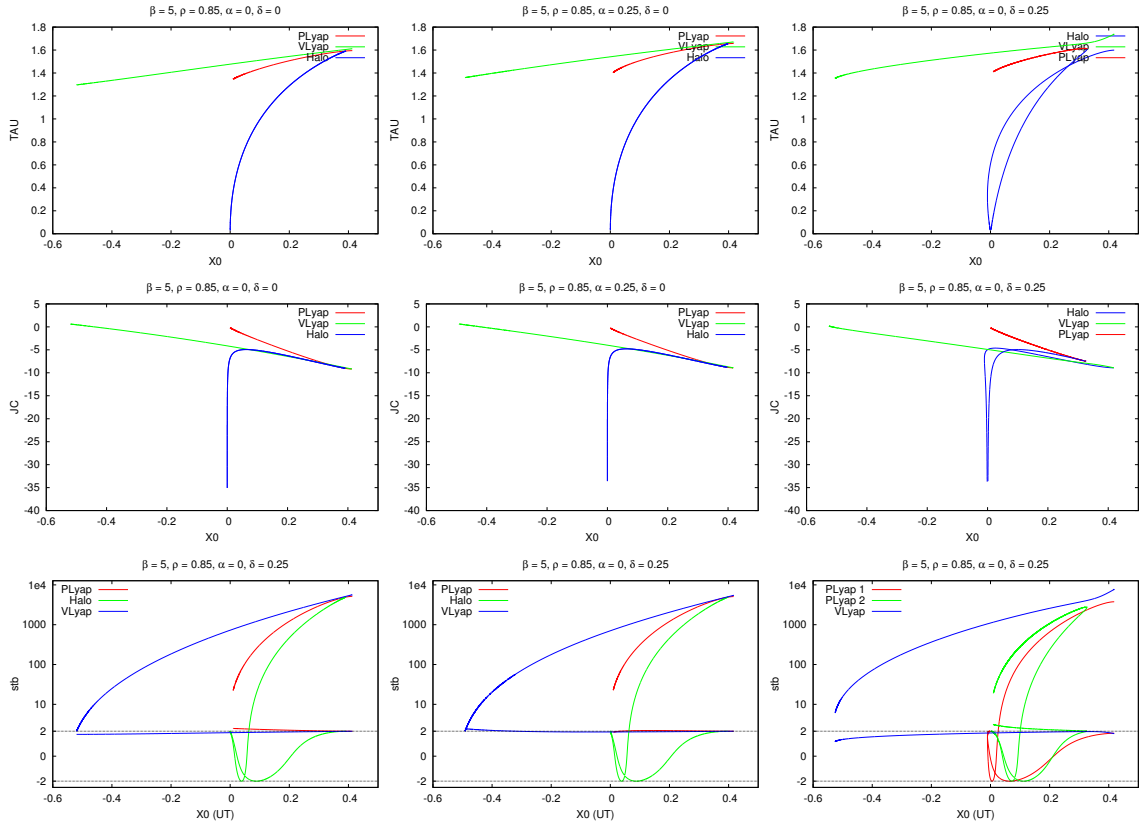
8

Figure 8. For $\bar{\beta} = 5, \rho = 0.85$, $(\alpha = 0,\ \delta = 0)$ **left,** $(\alpha = 0.25,\ \delta = 0)$ **middle and** $(\alpha = 0,\ \delta = 0.25)$ **right. Continuation diagrams of the families of periodic orbits: top** $x_0\ vs\ \tau$ **the orbital period, middle** $x_0\ vs\ J_c$ **jacobi constant, bottom** $x_0\ vs\ (s_1, s_2)$ **the stability parameters of the orbit.**

the other hand, the two linear oscillations give rise, in the full system, to two families of periodic orbits (the so-called Lyapunov periodic orbits), described in the previous section, plus a family of quasi-periodic motions (sometimes known as Lissajous orbits) with two basic frequencies.[13]

In this section we will describe the quasi-periodic motion for different sets of sail orientations. We will do this by means of two different techniques: reduction to the centre manifold and numerical computation of invariant tori. The centre manifold contains all the periodic and quasi-periodic motions near the equilibrium point and it is very useful to visualise the whole dynamics near the point. Reduction to the centre manifold is a semianalytical procedure and, as such, works in the neighborhood of the fixed point in which the expansions give accurate approximations. The numerical computation of families of quasi-periodic motions is a natural generalisation that allows to reach any energy, at the cost of a less global description.

Centre manifold near equilibria

The centre manifold at the equilibrium point is an invariant manifold that contains these periodic and quasi-periodic motions. In this case, this is a 4D manifold with a normally hyperbolic character due to the saddle part.

To visualise and study all the non-escaping orbits near this point we use the so-called reduction

to the centre manifold. The idea of this process is as follows. First, the origin of coordinates is translated to the equilibrium point. Then, a linear change of variables is used to uncouple the linear hyperbolic part from the elliptic one. After this transformation, the equations should look as

$$
\begin{aligned}
\dot{u} &= Au + O_2(u, v), \\
\dot{v} &= Bv + O_2(u, v),
\end{aligned}
$$

where A is an elliptic 4×4 matrix and B a hyperbolic 2×2 matrix. The idea is to go on with this uncoupling up to high orders in u and v. Hence, computing the Taylor expansion of the vector field at the equilibrium point, we obtain an expression like

$$
\begin{aligned}
\dot{u} &= Au + f(u, v), \\
\dot{v} &= Bv + g(u, v),
\end{aligned}
$$

where f and g are functions whose Taylor expansion starts with terms of second degree. Then, by means of a standard normal form scheme, we can apply near-identity changes of variables to suppress the monomials of the expansion that couple the elliptic directions to the hyperbolic ones, up to a given degree n. The resulting differential equation has the form

$$
\begin{aligned}
\dot{u} &= Au + f_n(u, v) + r_{n+1}^{(1)}(u, v), \\
\dot{v} &= Bv + g_n(u, v) + r_{n+1}^{(2)}(u, v),
\end{aligned}
$$

where A is an elliptic 4×4 matrix, B a hyperbolic 2×2 matrix, and f_n and g_n are polynomials of degree n such that $g_n(u, 0) = 0$. In other words, all the monomials of g that only depend on u have been suppressed. Note that, if we are close to the equilibrium point, the remainders $r_{n+1}^{(1,2)}$ are very small and, neglecting them, the manifold $v = 0$ becomes invariant. The dynamics on this manifold is described by the differential equation

$$
\dot{u} = Au + f_n(u, 0),
$$

and note that the hyperbolic behaviour has been removed. In these coordinates, $v = 0$ is the so-called centre manifold, and contains the periodic and quasi-periodic motions near the equilibrium point. Note that this is a 4D Hamiltonian system (i.e., with 2 degrees of freedom) whose dynamics can be easily visualised by fixing an energy level and plotting a 2D Poincaré section. All the trajectories displayed in this section are unstable in the full system due to the hyperbolic part that has been removed to compute the centre manifold.

It is not difficult to see that Equation (1) corresponds to a Hamiltonian system: defining momenta as usual, $P_X = \dot{X} - Y$, $P_Y = \dot{Y} + X$ and $P_Z = \dot{Z}$, the Hamiltonian function is given by

$$
H = \frac{1}{2}(P_X^2 + P_Y^2 + P_Z^2) + Y P_X - X P_Y - \frac{1}{2}(2X^2 - Y^2 - Z^2) - \frac{1}{r} - a_X X - a_Y Y - a_Z Z,
$$

where the values a_X, a_Y, a_Z are given in (3) and $r^2 = X^2 + Y^2 + Z^2$. Moreover, it is easy to check that $H = \frac{1}{2}J_C$.

Here we will take advantage of the Hamiltonian structure of the system, this is, all the transformations will be done on the Hamiltonian function instead of the differential equations. This means that, on one hand, the transformations have to be chosen canonical but, on the other hand, they need to be applied just to a single function, the Hamiltonian.[14, 15, 16]

Once the normalising process is finished (up to degree N), the remainder is neglected and the restriction of the Hamiltonian to the centre manifold takes the form

$$H_{cm} = H_2(q, p) + H_N(q, p),$$

where $q = (q_h, q_v)$, $p = (p_h, p_v)$, H_2 contains the second degree terms of the Hamiltonian and H_N contains monomials of degree between 3 and N. The second degree terms are of the form

$$H_2 = \frac{1}{2}\omega_h(q_h^2 + p_h^2) + \frac{1}{2}\omega_v(q_v^2 + p_v^2),$$

The frequencies $\omega_{h,v}$ correspond to linear oscillations around the point related to the horizontal and vertical Lyapunov orbits respectively. In all the cases studied here the frequencies $\omega_{h,v}$ are positive, which implies that, near the equilibrium point, the surfaces of level $H_{cm} = h$ are bounded (they look like deformed spheres). This also means that there are no trajectories near the equilibrium point with negative energy*and that, fixing a small energy level $h > 0$, the set of orbits with this energy must intersect the Poincaré section close to the origin.

The main limitation of this procedure is that we cannot describe the dynamics far from the equilibrium point. The reason is that it is computed as a power series at the equilibrium point so it is convergent up to the first singularity. The initial radius of convergence is the distance from the equilibrium point to the asteroid. This radius can be reduced by the normalising transformations but, in this case, as the normalising process does not have the so-called small divisors, the reduction of the radius of converge is almost unnoticeable.[15] This means that, in our case, the description is valid on a ball of centre the equilibrium point and radius the distance from this point to the asteroid.

To display the dynamics we have applied the following procedure. As before, let us call (q_h, p_h) the variables in the normalised coordinates related to the horizontal oscillations, and consider the Poincaré section $q_h = 0$ (in other words, we are "slicing" the vertical motions).

Let us consider the case $\alpha = \delta = 0$ and select the energy level $H_{cm} = 0.4$ (corresponding to $H = -4.519072$ in synodical coordinates). Take $q_h = 0$ as Poicaré section and, for a mesh of couples (q_v, p_v) we compute the (only) positive value of p_h such that $H_{cm}(0, p_h, q_v, p_v) = 0.4$ (if this value does not exist, it means that there are no orbits for this energy level crossing the section $q_h = 0$). Plotting the successive intersections of these orbits with $q_h = 0$ we obtain Figure 9. The point at the centre corresponds to a vertical periodic orbit (in this case, this is the vertical Lyapunov orbit corresponding to this energy level) and the curves around it correspond to quasi-periodic motions (Lissajous orbits). The outer boundary of this disk is given by the planar Lyapunov orbit.

Increasing the energy level up to $H_{cm} = 0.8$ ($H = -4.450858$ in synodical coordinates) we obtain Figure 10. Here one can see the two Halo orbits, surrounded by quasi-periodic motions (sometimes called quasi-Halos). In summary, for this sail orientation ($\alpha = \delta = 0$), the phase space near the equilibrium point looks very similar to the one of the classical RTBP.

Now let us consider the sail orientation to $\alpha = 0.1$ and $\delta = 0$. Near the new equilibrium point, the dynamics is very similar to the previous case. Increasing the energy level, the Halo orbits appear. Figure 11 shows the Poincaré section for the energy level $H_{cm} = 0.8$ ($H = -4.429012$ in synodical coordinates). We recall that, as we saw in the previous section, here we have a similar dynamics as

---

*This means that the energy of periodic (Lyapunov) and quasi-periodic (Lissajous) orbits near the equilibrium point must be larger than the energy at the equilibrium point.
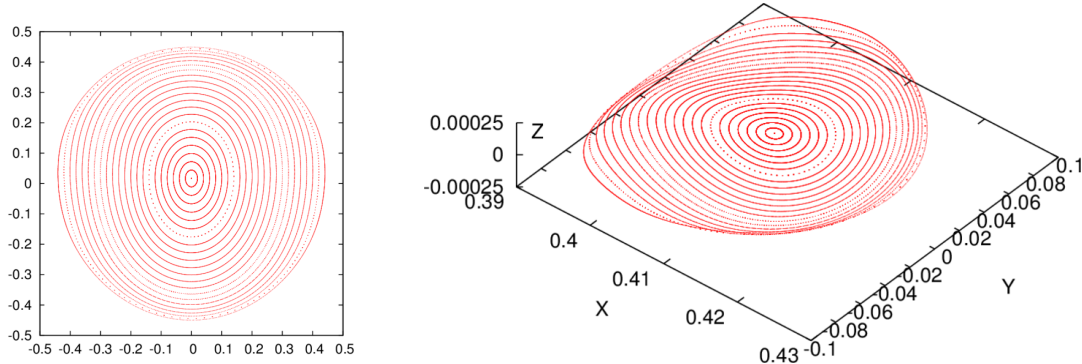
Figure 9. Centre manifold at the L_2 point for $\alpha = \delta = 0$ and $H_{cm} = 0.4$. **Left: Poincaré section in normalised coordinates (q_v, p_v). Right: The left plot in synodical coordinates.**
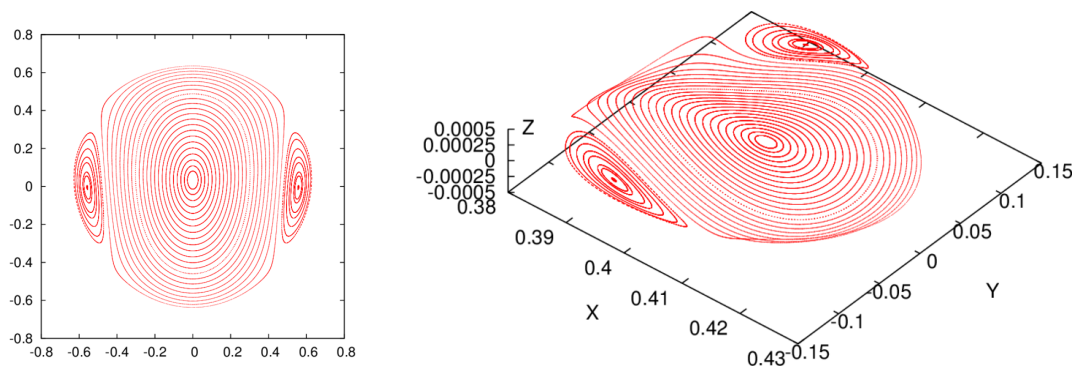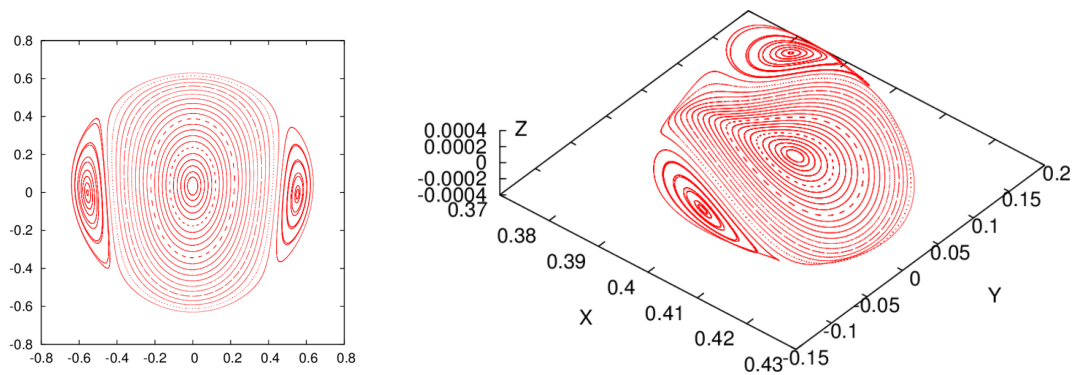

Figure 10. As Figure 9, but for $H_{cm} = 0.8$.

Figure 11. Centre manifold at the point L_2 for $\alpha = 0.1$, $\delta = 0$ and $H_{cm} = 0.8$. **Left: Poincaré section in normalised coordinates (q_v, p_v). Right: The left plot in synodical coordinates.**

for $\alpha = \delta = 0$, the main difference being that the orbits are shifted in the plane as it can also be seen here.

Finally, let us consider the sail orientation given by $\alpha = 0$ and $\delta = 0.1$. As in the previous cases, the dynamics for values of H_{cm} close to 0 is very similar to the one shown in Figure 9. For larger values of the energy, some bifurcations appear. For instance, Figure 12 shows the Poincaré section for $H_{cm} = 2.3$ ($H = -4.170575$ in synodical coordinates). In the left side, there is an small island (magnified in the right plot) that corresponds to one Halo orbit. If we move more to the right, we see a second elliptic orbit that corresponds to the vertical Lyapunov orbit and, moving more to the right, we see a couple of elliptic/hyperbolic orbits. The elliptic one is a Halo orbit, and the hyperbolic one is the planar Lyapunov orbit from which this Halo has branched off (compare with Figure 4 right). We have not included the section in synodical coordinates corresponding to the plots of Figure 12, since it is very similar to the previous ones.
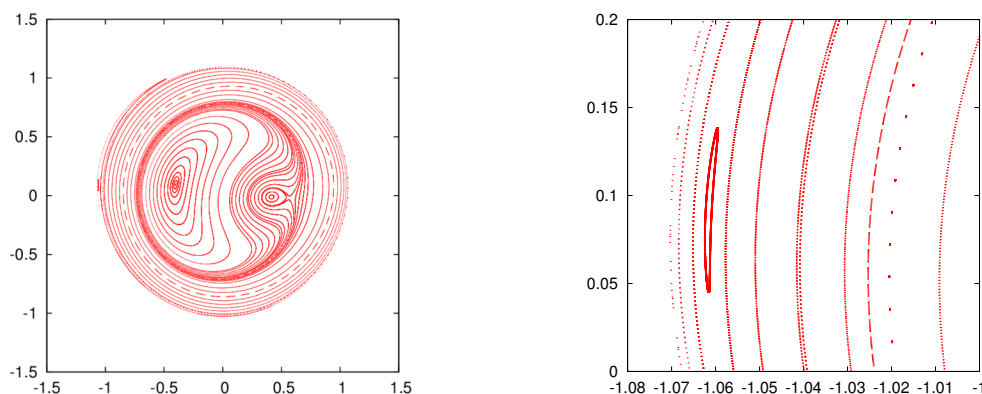

Figure 12. Centre manifold at the point L_2 for $\alpha = 0$, $\delta = 0.1$ and $H_{cm} = 2.3$. Left: Poincaré section in normalised coordinates. Right: Magnification of the left plot to show the island corresponding to a Halo orbit.

Invariant Tori

The Poincaré sections obtained in the previous sections are useful to visualise the existing quasi-periodic solutions near L_2. In this section we focus on the numerical computation of some of these quasi-periodic orbits. As it was mentioned previously, proceeding in this way we will be able to continue these families up to large distances from the equilibrium point, beyond the radius of convergence of the Taylor expansions used for the centre manifold.

The method used here is based on finding a curve inside the torus to be computed, invariant through the time–T flow, T being one of the periods of the torus, and approximated as a Fourier series.[17] Namely, denote the time–t flow (state transition map) as $\phi_t(x)$, where $x = (X, Y, Z, P_X, P_Y, P_Z)$ is a state of the AH3BP in Hamiltonian form. By an invariant torus we understand a geometrical object parameterised by a function $\psi(\theta_1, \theta_2)$ that is 2π–periodic in θ_1, θ_2 and satisfies

$$\phi_t\big(\psi(\theta_1, \theta_2)\big) = \psi(\theta_1 + t\omega_1, \theta_2 + t\omega_2),$$

where ω_1, ω_2 are the frequencies of the torus, so the corresponding periods are $2\pi/\omega_1, 2\pi/\omega_2$. In

13

order to find such a torus, we look for a parametrisation of a closed curve

$$\varphi(\theta) = A_0 + \sum_{k=0}^{N_f} \Big(A_k \cos(k\theta) + B_k \sin(k\theta) \Big)$$

satisfying the invariance equation

$$\phi_T\big(\varphi(\theta)\big) = \varphi(\theta + \rho) \tag{6}$$

for $\theta \in [0, 2\pi]$. Here ρ is called the *rotation number*. From the previous equation, a calculation shows that the function

$$\psi(\theta_1, \theta_2) = \phi_{T\theta_2/(2\pi)}\Big(\varphi\big(\theta_1 - \frac{\theta_2}{2\pi}\rho\big) \Big)$$

is 2π–periodic in θ_1, θ_2, and satisfies

$$\phi_t\big(\psi(\theta_1, \theta_2)\big) = \psi\big(\theta_1 + t(\rho/T), \theta_2 + t(2\pi/T)\big),$$

that is, the torus given by $\psi(\theta_1, \theta_2)$ is invariant with frequencies $\omega_1 = \rho/T$, $\omega_2 = 2\pi/T$.

In order to be solved numerically, equation (6) is discretised by taking values of θ equally spaced in $[0, 2\pi]$, as many as Fourier coefficients need to be determined (i.e. $1 + 2N_f$). This gives rise to a non–linear system of equations

$$\phi_T\big(\varphi(\theta_j)\big) = \varphi(\theta_j + \rho), \tag{7}$$

with $\theta_j = j2\pi/(1 + 2N_f)$, that is solved via Newton's method. In this system, the unknowns are the Fourier coefficients A_k, B_k as well as ρ, T. The families of tori we look for are two–parametric. This can be inferred from the Poincaré section plots of the centre manifold of the previous section, in which we can see a one–parametric family of tori at each energy level. We could use ρ, T as parameters, but the computations of the centre manifold suggest that the value of the Hamiltonian, or energy, is a better parameter. We will then add an energy equation to (7) and solve

$$\begin{aligned} H(\varphi(0)) &= h, \\ \phi_T\big(\varphi(\theta_j)\big) &= \varphi(\theta_j + \rho), \quad j = 0, \ldots, 2N_f, \end{aligned} \tag{8}$$

for h, T, ρ, A_k, B_k. This system can be used to follow families of tori using standard continuation procedures.[18] Since these procedures need the families to be 1–parametric, one of the parameters h, ρ needs to be fixed. There are some additional technical details, such as how to start continuations from central parts of periodic orbits.[19]

For each energy level in which there is a periodic orbit with central part, meaning that one of its stability parameters s_i is such that $|s_i| < 2$, a one–parametric family of invariant tori can be grown from the periodic orbit. Since this happens in a range of energy levels, families of invariant tori are 2–parametric. The families of Lissajous orbits shown in Figure 9 can be computed numerically as described before, either starting at the vertical Lyapunov orbit and ending at the planar one or vice-versa. For higher energy levels (as in Figure 10), in order to get Lissajous tori, we can only start from the vertical Lyapunov orbit, since the planar one has no central part (its stability parameters satisfy $|s_1|, |s_2| > 2$). Quasi-Halo tori have to be computed separately, starting from each of the two Halo orbits of the energy level.

For shortness, in this paper we only show invariant tori associated to the Lissajous family, and for $\alpha = \delta = 0$ (the tori with $\alpha \neq 0$ or $\delta \neq 0$ look similar but displaced, in the same way periodic orbits
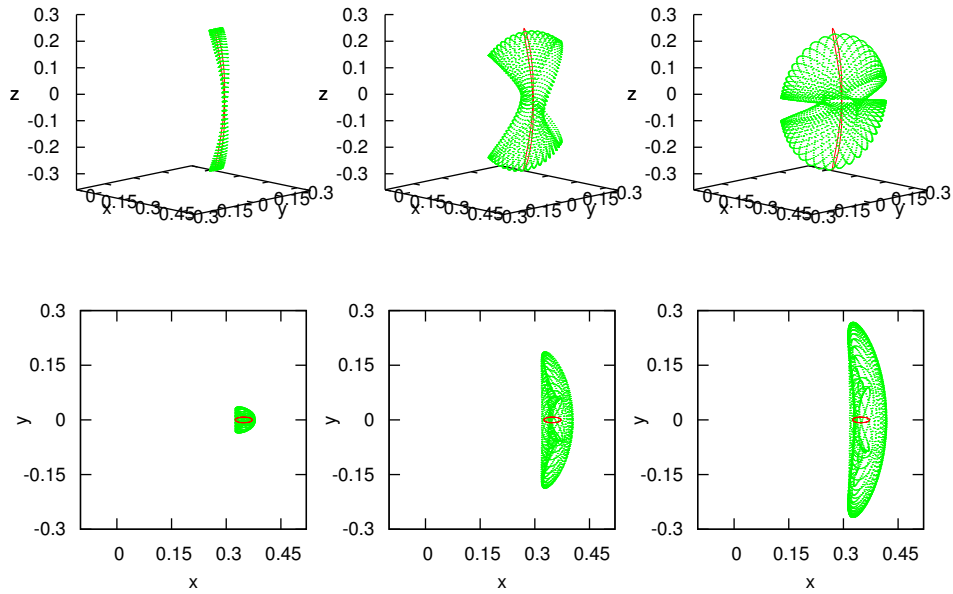
14

Figure 13. Several invariant tori (in green) around a vertical Lyapunov orbit (in red) for $H = -4.00280$, $\alpha = 0$, $\delta = 0$.
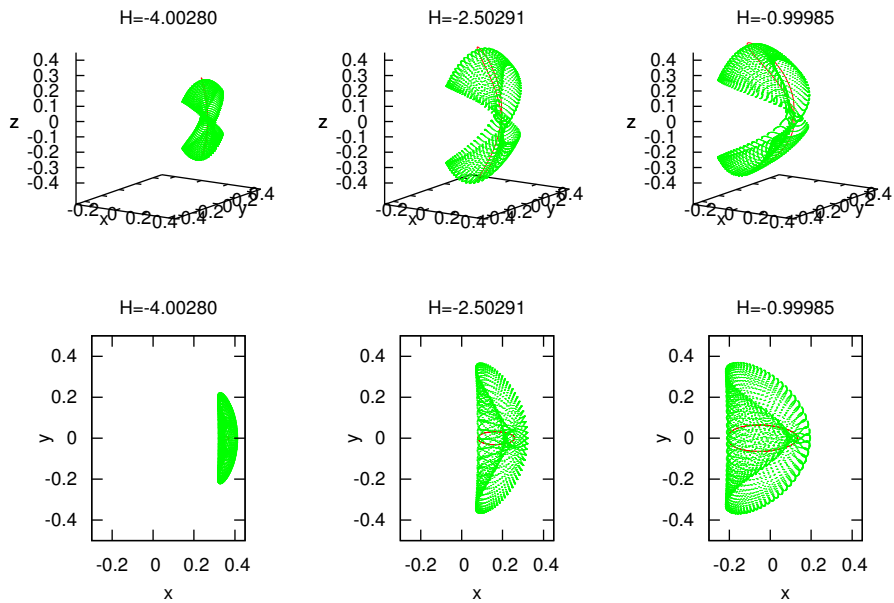

Figure 14. An invariant torus (in green) around the vertical Lyapunov orbit of the same energy (in red), for $\alpha = 0$, $\delta = 0$ and the energies indicated.

do). In order to compute these tori, we always start from vertical Lyapunov periodic orbits, since this family is the one that reaches higher energy levels with a center part, see Figure 8. Figure 13 shows, for $\alpha = \delta = 0$, three invariant tori corresponding to the energy level $H = -4.00280$, close but larger than the ones of the center manifold plots (Figures 9 to 12). The tori in Figure 13 are obtained from the vertical Lyapunov orbit corresponding to this energy level and by continuation of the system of equations (8) with respect to the rotation number ρ. From left to right, they are shown as produced by the continuation procedure. It can be seen how, as they gain Y amplitude, they contain orbits with ground tracks that exhibit lower latitudes. All three tori stay in the dark side of the asteroid, but, as vertical orbits do, for higher energies (Figure 14), their trajectories reach the Sun side, again with ground tracks with lower latitudes than vertical Lyapunov orbits. On the other hand, Figure 14 shows a torus for each of the three energy levels specified. These energy levels have been chosen in order to cover about half the family of vertical Lyapunov orbits (compare with Figure 6). Finally, let us add that all these invariant tori are unstable. A detailed study of their normal eigenvalues[20] is work in progress.

SOME ORBIT PROPERTIES RELEVANT IN A CERES MISSION SCENARIO

In the mission scenario of a solar sail close to Ceres, there are several restrictions that must be taken into account. For instance: orbiting close to the asteroid to allow more detailed scientific observations; keeping the solar sail almost perpendicular to the SRP to magnify the sail's performance; and being able to observe the day side of the asteroid.

In order to be close to Ceres, we must consider the equilibrium points and periodic orbits around the displaced L_2 equilibria. The main drawback of this region is that most of the periodic motion remains in the shadow side of the asteroid, which could compromise an observational mission. Nevertheless, we have found that some of the periodic orbits on the Planar and Vertical families spend part of their period on the day side of the asteroid, and could be interesting for an observational mission. Similar behaviour has been observed in quasi-terminator orbits[7] and we are working on relating these orbits to our work.

In Figures 15, 16 and 17 we summarise the % of the orbital period that the orbit spends in the day side and the maximum and minimum distance to the asteroid for each of the families of periodic orbits for the case: $(\alpha = 0, \delta = 0)$, $(\alpha = 0.25, \delta = 0)$ and $(\alpha = 0, \delta = 0.25)$ respectively.
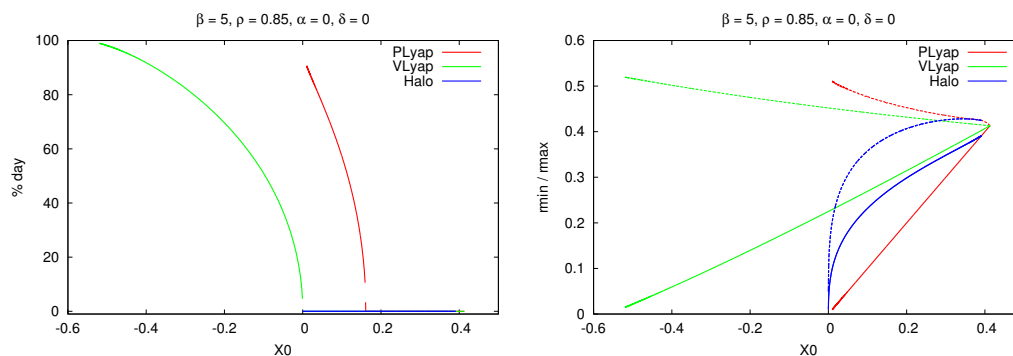

Figure 15. Properties of the families of periodic orbits for $\beta = 5, \rho = 0.85$, $(\alpha = 0, \delta = 0)$. **From left to right and top to bottom:** x_0 vs % **of the orbits period spent in the day side of the asteroid;** x_0 vs **minimum and maximum distance from the orbit to the asteroid;**
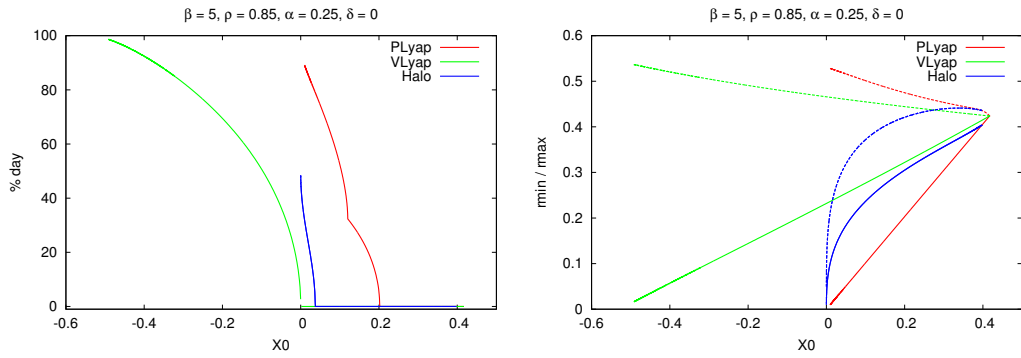
Figure 16. Properties of the families of periodic orbits for $\beta = 5, \rho = 0.85,$ ($\alpha = 0.25, \delta = 0$). **From left to right and top to bottom:** x_0 vs % **of the orbits period spent in the day side of the asteroid;** x_0 vs **minimum and maximum distance from the orbit to the asteroid;**
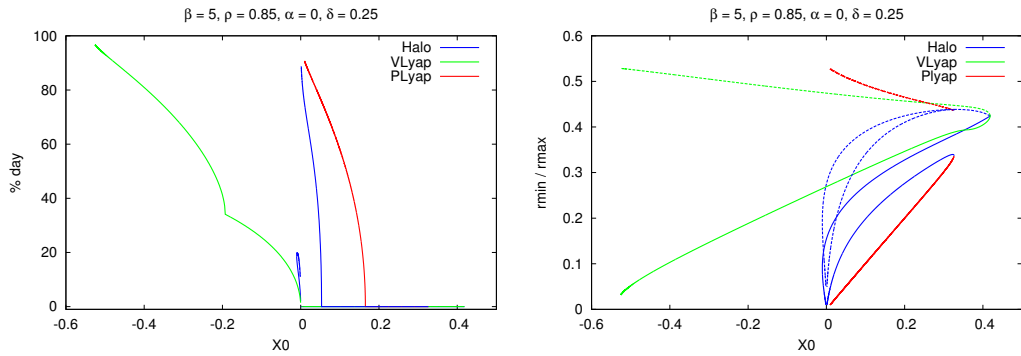

Figure 17. Properties of the families of periodic orbits for $\beta = 5, \rho = 0.85,$ ($\alpha = 0, \delta = 0.25$). **From left to right and top to bottom:** x_0 vs % **of the orbits period spent in the day side of the asteroid;** x_0 vs **minimum and maximum distance from the orbit to the asteroid;**

Notice how, as we move along the families of Planar and Vertical Lyapunov type of periodic orbits the maximum and minim distance to the asteroid differs a lot, having very close passages ($r_{min} \approx 5 \times 10^{-3}$UD (1609.8km) vs $r_{max} \approx 0.5$ UD (160983.3km) from the centre of Ceres). This can easily be understood by looking at the shape of both types of orbits (Figures 5 and 6).

If we look at the % of the period that the Planar and Vertical Lyapunov orbits spend on the day side, we can see that at some point the orbits spend more than the 50% of their time on the day side. The period of most of these orbits is ≈ 1.5UT (≈ 399 days), and the rotational period of Ceres is of 0.3781 days. This makes these orbits interesting for mission applications. Moreover, although we can see in Figure 8 that these orbits are unstable, we can also observe that their instability decreases drastically along the family.

When we look at the Halo-type orbits for a solar sail perpendicular to the Sun-asteroid line $\alpha = \delta = 0$, these orbits spend all of their time on the shadow side of the asteroid. Notice that if we shift the sail orientation, we find that some of these orbits do spend at most half of their period in the day side. The period of these orbits is between 0.1 and 0.5 UT (i.e. 26.6 and 133 days). Although they do not spend most of their time in the day side, the advantage of these terminator Halo-type orbits

17

is that they are stable and no station keeping would be required. Nevertheless, we should need to check how edged off do we see the asteroid from these orbits.

CONCLUSION

In this paper we have considered the AH3BP to model the dynamics of a solar sail close to an asteroid, and have considered as example an asteroid of the size of Ceres and a sail performance similar to NanoSail-D. For a fixed sail performance, here $\bar{\beta} = 5$ and $\rho = 0.85$, the system depends on two parameters α and δ that define the sail orientation. We have focused on the region around L_2 as it gets close to the asteroid when we include the SRP, and described some of the most relevant dynamical properties of the system depending on these two parameters (fixed points, periodic and quasi-periodic motion).

For each fixed sail orientation we have 3 types of families of periodic orbits: Planar and Vertical Lyapunov orbits and Halo-type orbits. These families are displaced with respect to the Sun-asteroid line depending on the sail orientation. We have used the reduction to the centre manifold to ensure that we have detected all the relevant trajectories: besides the periodic orbits there are Lissajous type orbits and quasi-Halo orbits. Next, we have computed explicitly some of these Lissajous type orbits. We are currently working in order to classify all the different types of quasi-periodic motion.

Finally, we have described some of the properties of the different families of periodic orbits that could be interesting for a mission application close to Ceres. We have found that some of the orbits spend more than half of their orbital period on the day side of the asteroid. Unfortunately, these orbits are unstable and a station keeping strategy should be used in order to stay close to them. In the near future we will deal with the controllability of these orbits. Given the instability rate and the orbital period of these orbits a station keeping strategy should be feasible.

ACKNOWLEDGEMENT

REFERENCES

[1] B. Dachwald, H. Boehnhardt, U. Broj, U. Geppert, J.-T. Grundmann, W. Seboldt, P. Seefeldt, P. Spietz, L. Johnson, E. Khrt, S. Mottola, M. Macdonald, C. McInnes, M. Vasile, and R. Reinhard, "Gossamer Roadmap Technology Reference Study for a Multiple NEO Rendezvous Mission," *Advances in Solar Sailing* (M. Macdonald, ed.), Springer Praxis Books, pp. 211–226, Springer Berlin Heidelberg, 2014.

[2] B. Villac, G. Ribalta, A. Farrés, À. Jorba, and J. Mondelo, "Using Solar Arrays for Orbital Control Near Small Bodies. Trade-offs Characterization.," *AIAA/AAS Astrodynamics Specialist Conference*, Minneapolis, Minnesota, 2012.

[3] E. Morrow, D. Scheeres, and D. Lubin, "Solar Sail Orbit Operations at Asteroids," *Journal of Spacecraft and Rockets*, Vol. 38, March–April 2001, pp. 279–286.

[4] M. Giancotti and R. Funase, "Solar Sail Equilibrium Positions and Transfer Trajectories close to a Trojan Asteroid," *Proceedings of the 63rd International Astronautical Congress*, 2012.

[5] Y. Katherine and B. Villac, "Periodic Orbits Families in the Hill's Three-Body Problem with Solar Radiation Pressure," *Advances in the Astronautical Sciences Series*, Vol. 136, San Diego, Colifornia, 2010.

[6] B. Dachwald, W. Seboldt, M. Macdonald, G. Mengali, A. Quarta, C. McInnes, L. Rios-Reyes, D. Scheeres, B. Wie, M. Görlich, *et al.*, "Potential Solar Sail Degradation Effects on Trajectory and Attitude Control," *AIAA Guidance, Navigation, and Control Conference and Exhibit*, Vol. 6172, 2005.

[7] S. B. Broschart, G. Lantoine, and D. J. Grebow, "Characteristics of quasi-terminator orbits near primitive bodies," *23rd AAS/AIAA Spaceflight Mechanics Meeting, Kauai, Hawaii*, 2013.

[8] A. Farrés, A. Jorba, J.-M. Mondelo, and B. Villac, "Periodic Motion for an Imperfect Solar Sail Near an Asteroid," *Advances in Solar Sailing* (M. Macdonald, ed.), Springer Praxis Books, pp. 885–898, Springer Berlin Heidelberg, 2014.

[9] K. Meyer and G. Hall, *Introduction to Hamiltonian Dynamical Systems and the N-Body Problem*. New York: Springer, 1992.

[10] C. Simó, "On the analytical and numerical approximation of invariant manifolds," *Modern methods in celestial mechanics* (D. Benest and C. Froeschlé, eds.), pp. 285–330, Ed. Frontières, 1990. Reprinted in http://www.maia.ub.es/dsg/2004/index.html.

[11] A. Farrés and À. Jorba, "Periodic and Quasi-Periodic motions of a Solar Sail around the family SL_1 on the Sun-Earth System," *Celestial Mechanics and Dynamical Astronomy*, Vol. 107, 2010, pp. 233–253.

[12] M. Hénon, "Exploration Numérique du Problème Restreint. II: Masses égales, stabilité des orbites periódiques," *Annales d'Astrophysique*, Vol. 28, No. 6, 1965, p. 992.

[13] À. Jorba and J. Villanueva, "On the normal behaviour of partially elliptic lower dimensional tori of Hamiltonian systems," *Nonlinearity*, Vol. 10, 1997, pp. 783–822.

[14] À. Jorba, "A methodology for the numerical computation of normal forms, centre manifolds and first integrals of Hamiltonian Systems," *Exp. Math.*, Vol. 8, No. 2, 1999, pp. 155–195.

[15] À. Jorba and J. Masdemont, "Dynamics in the centre manifold of the collinear points of the Restricted Three Body Problem," *Phys. D*, Vol. 132, 1999, pp. 189–213.

[16] A. Farrés and À. Jorba, "On the high order approximation of the centre manifold for ODEs," *Discrete Contin. Dyn. Syst. Ser. B*, Vol. 14, No. 3, 2010, pp. 977–1000.

[17] E. Castellà and À. Jorba, "On the vertical families of two-dimensional tori near the triangular points of the bicircular problem," *Celestial Mech. Dynam. Astronom.*, Vol. 76, No. 1, 2000, pp. 35–54.

[18] E. L. Algower and K. Georg, *Numerical continuation methods: an introduction*. Springer, 1990.

[19] G. Gómez and J. M. Mondelo, "The dynamics around the collinear equilibrium points of the RTBP," *Phys. D*, Vol. 157, No. 4, 2001, pp. 283–321.

[20] À. Jorba, "Numerical computation of the normal behaviour of invariant curves of n-dimensional maps," *Nonlinearity*, Vol. 14, No. 5, 2001, pp. 943–976.